



## Cite as

Nano-Micro Lett.  
(2021) 13:167Received: 28 April 2021  
Accepted: 12 July 2021  
© The Author(s) 2021

# Oxygen-Defect Enhanced Anion Adsorption Energy Toward Super-Rate and Durable Cathode for Ni–Zn Batteries

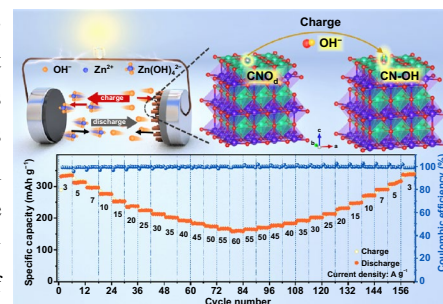
Jia Yao<sup>1</sup>, Houzhao Wan<sup>1</sup> ✉, Chi Chen<sup>2,3</sup> ✉, Jie Ji<sup>1</sup>, Nengze Wang<sup>1</sup>, Zhaohan Zheng<sup>1</sup>, Jinxia Duan<sup>1</sup>, Xunying Wang<sup>1</sup>, Guokun Ma<sup>1</sup>, Li Tao<sup>1</sup>, Hanbin Wang<sup>1</sup>, Jun Zhang<sup>1</sup>, Hao Wang<sup>1</sup> ✉

## HIGHLIGHTS

- Ultra-thin CoNiO<sub>2</sub> nanosheet with rich oxygen defects anchored on the vertically arranged Ni nanotube arrays (O<sub>d</sub>-CNO@Ni NTs) is successfully constructed.
- The O<sub>d</sub>-CNO@Ni NTs electrode delivers extraordinary electrochemical performance.
- The theoretical calculations reveal that oxygen defects effectively improve the electrochemical kinetics and the surface electronic state structure of O<sub>d</sub>-CNO @ Ni NTs, thus exhibiting strong OH<sup>−</sup> adsorption capacity.

**ABSTRACT** The alkaline zinc-based batteries with high energy density are becoming a research hotspot. However, the poor cycle stability and low-rate performance limit their wide application. Herein, ultra-thin CoNiO<sub>2</sub> nanosheet with rich oxygen defects anchored on the vertically arranged Ni nanotube arrays (O<sub>d</sub>-CNO@Ni NTs) is used as a positive material for rechargeable alkaline Ni–Zn batteries. As the highly uniform Ni nanotube arrays provide a fast electron/ion transport path and abundant active sites, the O<sub>d</sub>-CNO@Ni NTs electrode delivers excellent capacity (432.7 mAh g<sup>−1</sup>) and rate capability (218.3 mAh g<sup>−1</sup> at 60 A g<sup>−1</sup>). Moreover, our O<sub>d</sub>-CNO@Ni NTs//Zn battery is capable of an ultra-long lifespan (93.0% of initial capacity after 5000 cycles), extremely high energy density of 547.5 Wh kg<sup>−1</sup> and power density of 92.9 kW kg<sup>−1</sup> (based on the mass of cathode active substance). Meanwhile, the theoretical calculations reveal that the oxygen defects can enhance the interaction between electrode surface and electrolyte ions, contributing to higher capacity. This work opens a reasonable idea for the development of ultra-durable, ultra-fast, and high-energy Ni–Zn battery.

**KEYWORDS** Ni–Zn battery; Oxygen defect; Nanotube array; CoNiO<sub>2</sub> nanosheet; Adsorption energy



✉ Houzhao Wan, houzhao@hubu.edu.cn; Chi Chen, xmchenchi@fjirsm.ac.cn; Hao Wang, wangh@hubu.edu.cn; nanoguy@126.com

<sup>1</sup> Hubei Key Laboratory of Ferro and Piezoelectric Materials and Devices, School of Microelectronics and Faculty of Physics and Electronic Science, Hubei University, Wuhan 430062, People's Republic of China

<sup>2</sup> CAS Key Laboratory of Design and Assembly of Functional Nanostructures, and Fujian Provincial Key Laboratory of Nanomaterials, Fujian Institute of Research on the Structure of Matter, Chinese Academy of Sciences, Fuzhou 350002, People's Republic of China

<sup>3</sup> Xiamen Key Laboratory of Rare Earth Photoelectric Functional Materials, Xiamen Institute of Rare Earth Materials, Haixi Institute, Chinese Academy of Sciences, Xiamen 361021, People's Republic of China



## 1 Introduction

With the increasing demand for green and sustainable energy storage, advanced energy storage technology like lithium-ion batteries (LIBs) has attracted extensive attentions [1–3]. However, their applications are seriously hindered caused by the Li dendrite formation and the side reactions, which could cause serious degradation and safety problems [4–6]. As an alternative to LIBs, rechargeable alkaline Zn-based batteries (ZBBs) have attracted more and more attentions with high theoretical capacity ( $820 \text{ mAh g}^{-1}$ ), low cost, high security, and good ionic conductivity [7, 8].

To date, various alkaline Zn-based cathodes have been developed, such as  $\text{MnO}_2$  [9], Ag-based [10], and Ni, Co-based materials (e.g.,  $\text{Ni(OH)}_2$  [11, 12],  $\text{NiO}$  [13],  $\text{NiSe}_2$  [14],  $\text{Ni}_3\text{S}_2$  [15, 16],  $\text{Co}_3\text{O}_4$  [17–19],  $\text{Co}_3\text{S}_4$  [20],  $\text{NiCo-DH}$  [21, 22], and  $\text{NiCo}_2\text{O}_4$  [23–25]). While  $\text{MnO}_2$ -Zn battery has a low working voltage and weak stability,  $\text{AgO-Zn}$  battery has low stability, poor overcharge tolerance and high cost. Conversely, Ni-Zn batteries (NZBs) have the advantages of high energy density and high output voltage, reversible oxidation–reduction kinetics of Zn/ZnO, low cost and low toxicity, etc. [26]. However, currently reported cathode materials have low cycle stability due to the self-dissolution of the cathode, the corrosion and dendrite formation of the anode, etc. [27]. Thus, the further development of NZBs is severely restricted.

To address the above limitations, many strategies, including structural design, metal ions doping and surface properties optimization, have been attempted (summarized in Table S1) [28, 29]. Structural design is used to strengthen the electrochemical performance of electrode materials. For example, Chao et al. reported that the  $\text{NiS@Ni}_{0.95}\text{Zn}_{0.05}(\text{OH})_2$  used in NZBs has a long life and fast energy response ( $18.82 \text{ kW kg}^{-1}$ , peak power output of 30 s) [30]. Ionic doping could promote the transmission of ions/electrons and show more redox reactions, thereby contributing to electrochemical performance [31]. Surface modification with the introduction of defects and higher conductivity additives, the surface reactivity and reaction kinetics of electrode materials are improved [32]. Lu et al. reported a mesoporous nanostructured  $\text{Co}_3\text{O}_4$  with oxygen defects as the cathode of ZBBs, providing an excellent

long-life performance (the capacity does not decrease after 60,000 cycles) [19]. However, the energy density and cycle lifespan of the NZBs are still far from up to standard for practical applications due to the poor conductivity, limited exposure to active sites, and large volume variations for cathode materials. In summary, the exploration of cathode materials with ultra-high capacity, high rate capability and long life is still full of challenges and desirability.

Nickel cobaltate has superior electrochemical activity than oxides of single metal nickel or cobalt due to the electronic transition between the different valence states of the elements and the existence of  $\text{Co}^{3+}/\text{Co}^{2+}$  and  $\text{Ni}^{3+}/\text{Ni}^{2+}$  redox pairs [33]. Shang et al. prepared porous  $\text{NiCo}_2\text{O}_4$  nanosheets, nanowires and nanoplates as cathode of NZBs, which promoted electron transfer and electrochemical reaction, thereby showing excellent electrochemical performance [24]. However, the volume expansion of  $\text{CoNiO}_2$  (CNO) cathode during the charge–discharge, resulting in poor connection of the electron transmission channel and greatly reduced electrical conductivity, thus making its capacity and high-rate performance far from expected. Herein, we develop an unprecedented composite material that combines electrochemically active structures and defect engineering. Ultra-thin  $\text{CoNiO}_2$  nanosheets with abundant oxygen defects ( $\text{O}_d$ -CNO) are introduced in situ on the surface of vertically arranged Ni nanotube arrays (Ni NTs). The density functional theory (DFT) reveals that the introduction of oxygen defects can enhance the adsorption energy of  $\text{OH}^-$ , thereby improving the cycle stability of the crystal structure during charge–discharge. Simultaneously, the oxygen defects can effectively modulate the surface electronic structure to promote charge storage. As a consequence, the  $\text{O}_d$ -CNO@Ni NTs electrode shows excellent rate performance and high specific capacity. Concretely, the assembled  $\text{O}_d$ -CNO@Ni NTs//Zn rechargeable battery provides a capacity of  $334.9 \text{ mAh g}^{-1}$  and has long cycle life (93.0% retention after 5000 times). In addition, the Ni-Zn battery achieves an energy density of  $547.5 \text{ Wh kg}^{-1}$  and power density of  $92.9 \text{ kW kg}^{-1}$ . Encouragingly, even after the brutal treatment of hammer and fire, it still shows excellent reliability and safety. This study shows that  $\text{O}_d$ -CNO@Ni NTs//Zn has high practical application potential in high-performance ZBBs.

## 2 Experimental

### 2.1 Material Synthesis

#### 2.1.1 Fabrication of Ni NTs@Ni Foam

To obtain regular Ni NTs, the Ni NTs@ZnO array must be synthesized. First,  $\text{Zn}(\text{CH}_3\text{COO})_2 \cdot 2\text{H}_2\text{O}$  was dissolved in 100 mL anhydrous methanol ( $\text{CH}_3\text{OH}$ ), and nickel foam was placed in the solution and stirred by ultrasound, and then stored at 200 °C for 2 h. Secondly, 0.1 M  $\text{Zn}(\text{NO}_3)_2 \cdot 6\text{H}_2\text{O}$ , 0.1 M HMTA ( $\text{C}_6\text{H}_{12}\text{N}_4$ ), 0.1 M ammonia and nickel foam were transferred to a 100 mL Teflon-lined stainless steel, heated at 90 °C for 10 h. Then, Ni films were electrodeposited on ZnO nanorods arrays in 0.2 M  $\text{NiSO}_4 \cdot 6\text{H}_2\text{O}$  and 0.01 M  $\text{NH}_4\text{Cl}$  solutions at  $-1.5 \text{ mA cm}^{-2}$  for 12 min. After a further immersion in 0.01 M HCl solution for 5–10 min, the prepared sample is cleaned repeatedly with deionized water and dried.

#### 2.1.2 Fabrication of $\text{O}_d\text{-CNO@Ni NTs}$ , $\text{O}_d\text{-CNO}$ and CNO

According to our previous report, a cobalt-based organic skeleton (Co-MOF@Ni NTs) supported on Ni NTs was prepared [31]. In a typical experiment, 4 M 2-methylimidazole ( $\text{C}_4\text{H}_6\text{N}_2$ ) solution was quickly added to 0.05 M  $\text{Co}(\text{NO}_3)_2 \cdot 6\text{H}_2\text{O}$  solution, and then the prepared Ni nanotube arrays (Ni NTs) were infiltrated and grown for 4 h. The prepared Co-MOF@Ni NTs were immersed in 16 mM  $\text{NiSO}_4 \cdot 6\text{H}_2\text{O}$  solution, react at room temperature for 90 min, wash and dry to obtain NiCo-DH@Ni NTs. To obtain  $\text{O}_d\text{-CNO@Ni NTs}$ , the prepared sample was heated to 350 °C in the Ar environment for 2 h (heating rate of  $2 \text{ }^\circ\text{C min}^{-1}$ ). In the absence of Ni NTs, the NiCo-DH sample was heated to 350 °C in Ar atmosphere for 2 h (heating rate of  $2 \text{ }^\circ\text{C min}^{-1}$ ) to obtain the  $\text{O}_d\text{-CNO}$  sample. Similarly, the NiCo-DH sample was heated in air to 350 °C and held for 2 h (heating rate of  $2 \text{ }^\circ\text{C min}^{-1}$ ) to obtain CNO. The sample loading capacity is about 0.8–1.2  $\text{mg cm}^{-2}$ .

### 2.2 Material Characterization

The morphology and size were studied by scanning electron microscopy (SEM, JEOL JSM-7100F), transmission electron microscopy (TEM), high-resolution TEM (HRTEM) and selected area electron diffraction (SAED). Elemental analysis and morphology measurements were obtained by energy-dispersive X-ray spectrometer (EDX). The structure and chemical composition were characterized by X-ray diffraction (XRD; Bruker D8 Advance diffractometer), X-ray photoelectron spectrometer (XPS; Thermo Fisher Scientific Escalab 250Xi) and electron paramagnetic resonance (EPR; Bruker EMPplus-10/12). The  $\text{N}_2$  adsorption–desorption isotherms were measured by ASAP 2020 analyzer. The Co ion dissolved amount in the electrolyte was tested by the inductively coupled plasma optical emission spectrometry (ICP – OES).

### 2.3 Electrochemical Measurements

In this experiment, the electrochemical performance of Ni–Zn alkaline battery in a mixture of 4 M KOH + 1 M  $\text{K}_2\text{CO}_3$  + 2 M KF and saturated ZnO,  $\text{O}_d\text{-CNO@Ni NTs}$  and commercial zinc were used as cathode and anode, respectively. The Chenhua electrochemical workstation (CHI760E) was used for cyclic voltammetry (CV), galvanostatic charge–discharge (GCD) and electrochemical impedance spectroscopy (EIS) tests. Rate performance and cycle life were measured using the NEWARE battery test system (NEWARE, PR China). In the three-electrode electrochemical test using CHI760E, the nickel foam containing active material was directly prepared as working electrode, and saturated calomel electrode (SCE) was used as the reference electrode and platinum electrode (Pt) was used as the counter electrode.

The energy density  $E$  ( $\text{Wh kg}^{-1}$ ) and power density  $P$  ( $\text{kW kg}^{-1}$ ) are obtained by following:

$$E = \frac{I \int U dt}{m} \quad (1)$$

$$P = \frac{E}{t} \quad (2)$$

where  $I$  is the discharge current (mA),  $U$  is the discharge voltage (V),  $t$  is the discharge time (h), and  $m$  is the mass load of the active materials (mg).

## 2.4 Calculation Methods

The first-principle calculations are performed using VASP code [34], based on density functional theory (DFT) [35, 36]. The CNO slab with (001) surface is chosen as calculation model. The  $a$  and  $b$  axes are  $8.94 \text{ \AA} \times 8.94 \text{ \AA}$ , while the  $c$  axes are set to  $35 \text{ \AA}$  to ensure sufficient vacuum to avoid interactions between two cycles. By using the Perdew–Burke–Erzenhoff (PBE) exchange–correlation functional, the general gradient approximation (GGA) is used to calculate the exchange–correlation energy [37]. The DFT + U method [38, 39] with strong correlation effects was adopted to describe the localization of Co-3d and Ni-3d electrons. The U–J values of Co and Ni are 3.4 and 6.0 eV, respectively [40]. The influence of van der Waals interactions was estimated, and the optimal commutative van der Waals function DFT-D3 is realized [41]. The cutoff

energy of the plane wave was 500 eV, and the  $3 \times 3 \times 1$  and  $5 \times 5 \times 1$  k-point grids in the Monkhorst Pack [42] sampling scheme were used for geometric optimization and computation of electronic properties, respectively. The convergence condition of energy is  $10^{-4}$  eV, and the structures were relaxed until the force on each atom is less than  $0.03 \text{ eV \AA}^{-1}$ . Spin polarization is taken into account in all calculations, and structure mapping and charge density visualization were performed using VESTA [43].

The binding energies  $E_b$  of OH ion on the surfaces of CNO are defined as:

$$E_b = E_{\text{CNO} + \text{OH}} - (E_{\text{CNO}} + E_{\text{OH}}) \quad (3)$$

$$E_{\text{OH}} = E(\text{H}_2\text{O}) - 1/2E(\text{H}_2) \quad (4)$$

here,  $E_{\text{CNO} + \text{OH}}$  is the total energy of the CNO slab with an adsorbed OH,  $E_{\text{CNO}}$  is the total energy of pristine CNO slab and  $E_{\text{OH}}$  is the total energy of OH. And  $E(\text{H}_2\text{O})$  and  $E(\text{H}_2)$  are the total energy of  $\text{H}_2\text{O}$  and  $\text{H}_2$  molecule, respectively.

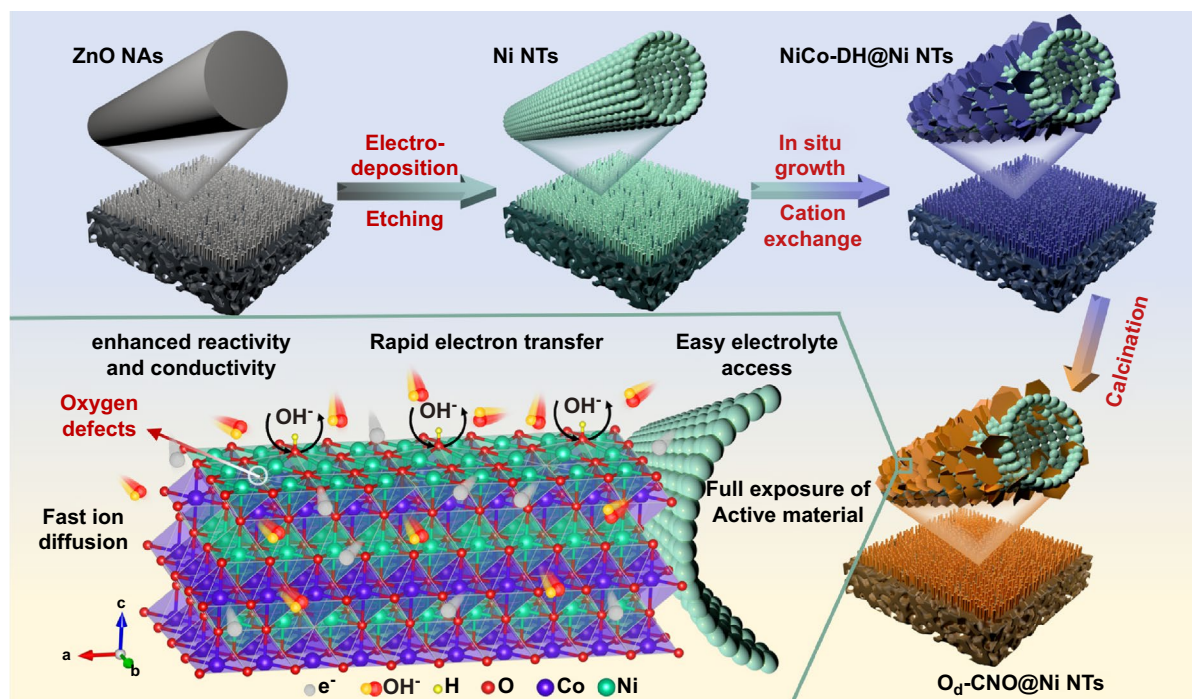


**Fig. 1** Synthesis mechanism of  $\text{O}_d\text{-CNO@Ni NTs}$  nanostructure

### 3 Results and Discussion

#### 3.1 Morphology and Structure

Ultra-thin  $\text{CoNiO}_2$  nanosheets with oxygen defects were prepared on nickel nanotubes ( $\text{O}_d\text{-CNO@Ni NTs}$ ) as the cathode material by cation exchange method. The principle of the preparation process is shown in Fig. 1. Firstly, ZnO nanorod arrays (ZnO NAs) were grown on pure nickel foam by hydrothermal method (Fig. S1a–c). The XRD peaks are well retrieved (PDF No. 36-1451, Fig. S1d). Then, uniform Ni films are electrodeposited. ZnO NAs were removed by etching, remaining the Ni NTs with hollow structures (PDF No. 04-0850, Figs. 2a and S2). Finally, the  $\text{O}_d\text{-CNO}$

nanosheet was prepared by in situ growth on Ni NTs. The Ni NTs are uniformly coated by interconnected ultra-thin  $\text{O}_d\text{-CNO}$  nanosheets (Fig. 2b), and the size of a single nanosheet was about 200 nm. As a comparison, SEM images of CNO and  $\text{O}_d\text{-CNO}$  samples are shown in Fig. S3. In addition, the Brunauer–Emmett–Teller (BET) results further demonstrate the high specific surface area of  $\text{O}_d\text{-CNO@Ni NTs}$  (Fig. S4). Specifically, the specific surface area of  $\text{O}_d\text{-CNO@Ni NTs}$  ( $52.25 \text{ m}^2 \text{ g}^{-1}$ ) was much higher than that of  $\text{O}_d\text{-CNO}$  ( $36.57 \text{ m}^2 \text{ g}^{-1}$ ) and CNO ( $35.84 \text{ m}^2 \text{ g}^{-1}$ ). The  $\text{O}_d\text{-CNO@Ni NTs}$  composite arrays combine the advantages of self-supporting Ni NTs and the abundant active sites of the  $\text{O}_d\text{-CNO}$  two-dimensional ultra-thin nanosheets, which

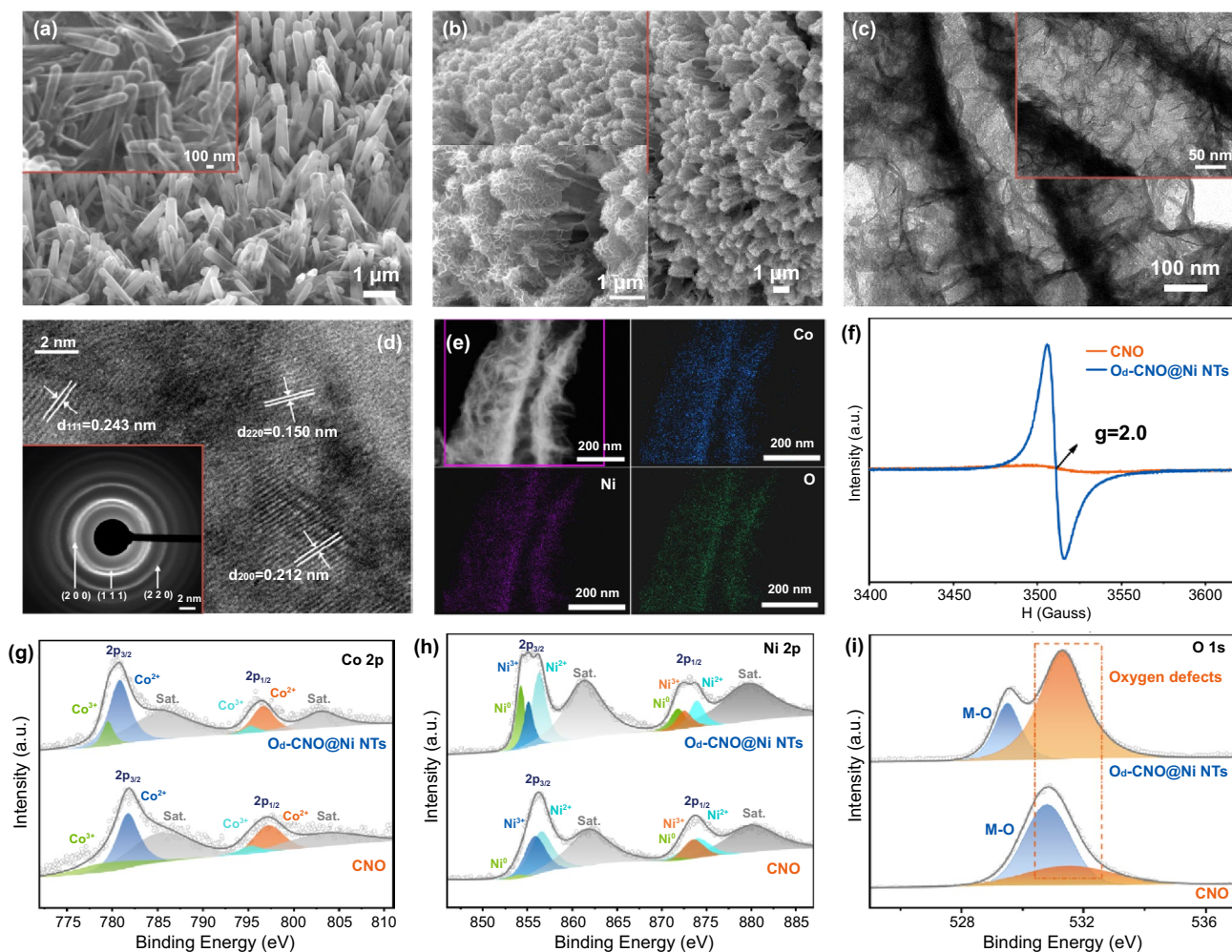


**Fig. 2** Structure characterization of  $\text{O}_d\text{-CNO@Ni NTs}$ . **a, b** SEM at high and low magnifications of Ni NTs and  $\text{O}_d\text{-CNO@Ni NTs}$ . **c** TEM images and **d** HRTEM images of  $\text{O}_d\text{-CNO@Ni NTs}$ . **e** EDX element mappings of  $\text{O}_d\text{-CNO@Ni NTs}$ . **f** EPR spectra of  $\text{O}_d\text{-CNO@Ni NTs}$ . **g–i** XPS of Co 2p, Ni 2p, and O 1s for  $\text{O}_d\text{-CNO@Ni NTs}$  and CNO

not only provides more active sites, but also reduces the ion transport distance [44].

To explore the structural differences caused by the introduction of oxygen defects, we also prepared CNO without oxygen defects (Fig. S5). Three diffraction peaks can be assigned to the (111), (200), and (220) crystal faces of CNO (PDF No. 10-0188) [45]. However, the intensity of diffraction peaks of the three main crystal planes of O<sub>d</sub>-CNO is weakened, which means that the crystallinity is weakened to some extent [23]. To further understand the microstructure of the samples, TEM was used to characterize. Figure 2c reveals the diameter of the Ni NTs is approximately 100 nm. The lattice fringes can be seen under HRTEM (Fig. 2d). Concretely, compared with CNO, the lattice fringe spacing of O<sub>d</sub>-CNO has no significant change, which is  $d_{(111)} = 0.243$  nm,  $d_{(200)} = 0.211$  nm, and  $d_{(220)} = 0.150$  nm, respectively. This corresponds to three faintly bright diffractive concentric rings in the SAED pattern (illustration of Fig. 2d), while that of CNO (Fig. S6) are clearer and brighter. As a result, this is consistent with the abovementioned characterization result in Fig. S5. According to the energy-dispersive EDX of O<sub>d</sub>-CNO@Ni NTs in Fig. 2e, Ni, Co, and O are evenly distributed on the nanosheet (Fig. S7 and Table S2). The optical photograph of the composite electrode also shows the uniform distribution of the electrode material on the nickel foam (Fig. S8).

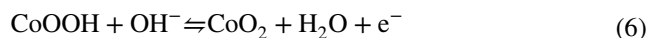
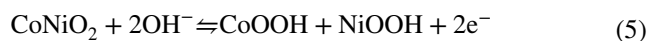
The results of electron paramagnetic resonance (EPR) analysis (Fig. 2f), the oxygen defects characteristic (g factor is a peak signal of 2.0) was generated in O<sub>d</sub>-CNO@Ni NTs lattice [46]. To further prove the existence of oxygen defects and analyze the valence state of each element, the XPS analysis of O<sub>d</sub>-CNO@Ni NTs was carried out. The XPS survey spectrum (Fig. S9) shows Co, Ni, O, and C, which are the main elemental of O<sub>d</sub>-CNO@Ni NTs. Figure 2g demonstrates two typical Co 2p<sub>1/2</sub> and Co 2p<sub>3/2</sub> orbitals of the CNO phase. It shows that the Co state exists in the form of Co<sup>2+</sup> and Co<sup>3+</sup> [47]. The Ni 2p emission spectra of the CNO and O<sub>d</sub>-CNO@Ni NTs samples (Fig. 2h) show Ni 2p<sub>1/2</sub> and Ni 2p<sub>3/2</sub> of spin-orbit doublets [48]. For O<sub>d</sub>-CNO@Ni NTs, the peak intensity of Ni<sup>3+</sup> is obviously weakened, and the binding energies are 855.2 and 872.9 eV, respectively, while the intensity of Ni<sup>2+</sup> with binding energies of 856.5 and 873.9 eV is increased, indicating that the reduction of Ni<sup>3+</sup> to Ni<sup>2+</sup> is related to sintering and annealing, thus confirming the generation of oxygen defects. In addition to Ni<sup>2+</sup> and Ni<sup>3+</sup>, Ni<sup>0</sup> exists in the valence state of Ni, indicating

that there are metallic Ni phase spots in O<sub>d</sub>-CNO@Ni NTs. It is easy to understand that the detected Ni<sup>0</sup> is mainly the presence of elemental nickel in the foamed nickel substrate and part of Ni NTs. Figure 2i is a comparative O 1s XPS spectrum of CNO and O<sub>d</sub>-CNO@Ni NTs samples. The peak intensity (M–O) at 529.8 eV mainly corresponds to the host lattice oxygen in O<sub>d</sub>-CNO@Ni NTs (Co–O/Ni–O). In particular, a more obvious peak intensity appears at 531.3 eV, which is related to the bonding state of the defect O [49].

### 3.2 Electrochemical Performance of the Electrode

The O<sub>d</sub>-CNO@Ni NTs electrochemical performance was characterized in a three-electrode system with 4 M KOH. Figure 3a shows the CV of Ni NTs, CNO, O<sub>d</sub>-CNO, and O<sub>d</sub>-CNO@Ni NTs were collected at 5.0 mV s<sup>-1</sup> (−0.1~0.6 V). The O<sub>d</sub>-CNO@Ni NTs electrode has a larger CV scanning area and higher response current (4.8 A g<sup>-1</sup> of Ni NTs, 30.2 A g<sup>-1</sup> of CNO, 40.5 A g<sup>-1</sup> of O<sub>d</sub>-CNO, 78.8 A g<sup>-1</sup> of O<sub>d</sub>-CNO@Ni NTs), which confirms its higher capacity storage and electrochemical activity. This may be associated with the promotion of surface charge state and the enhancement of OH<sup>-</sup> adsorption energy caused by oxygen defects. Besides, compared with CNO, the potential difference of cathodic peak and anodic peak of O<sub>d</sub>-CNO and O<sub>d</sub>-CNO@Ni NTs is much smaller, implying a lower electrochemical polarization for O<sub>d</sub>-CNO or O<sub>d</sub>-CNO@Ni NTs. The CV area of the Ni NTs electrode is quite small, which indicates that the Ni NTs electrode has almost no capacity contribution. CV curves for O<sub>d</sub>-CNO@Ni NTs electrodes from 2 to 60 mV s<sup>-1</sup> (Fig. 3b), their good symmetrical distribution and similar shape indicate the stability and reversibility of the electrode. The extremely high current density of O<sub>d</sub>-CNO@Ni NTs electrodes indicates its excellent high-power potential.

To study the electrochemical kinetics of O<sub>d</sub>-CNO@Ni NTs electrodes, a typical couple of redox peaks match the adsorption/desorption process of OH<sup>-</sup> in the redox reaction. The specific reaction equation can be described as:



The diffusion-controlled redox reaction is revealed by the relation between the peak current density and scan rate

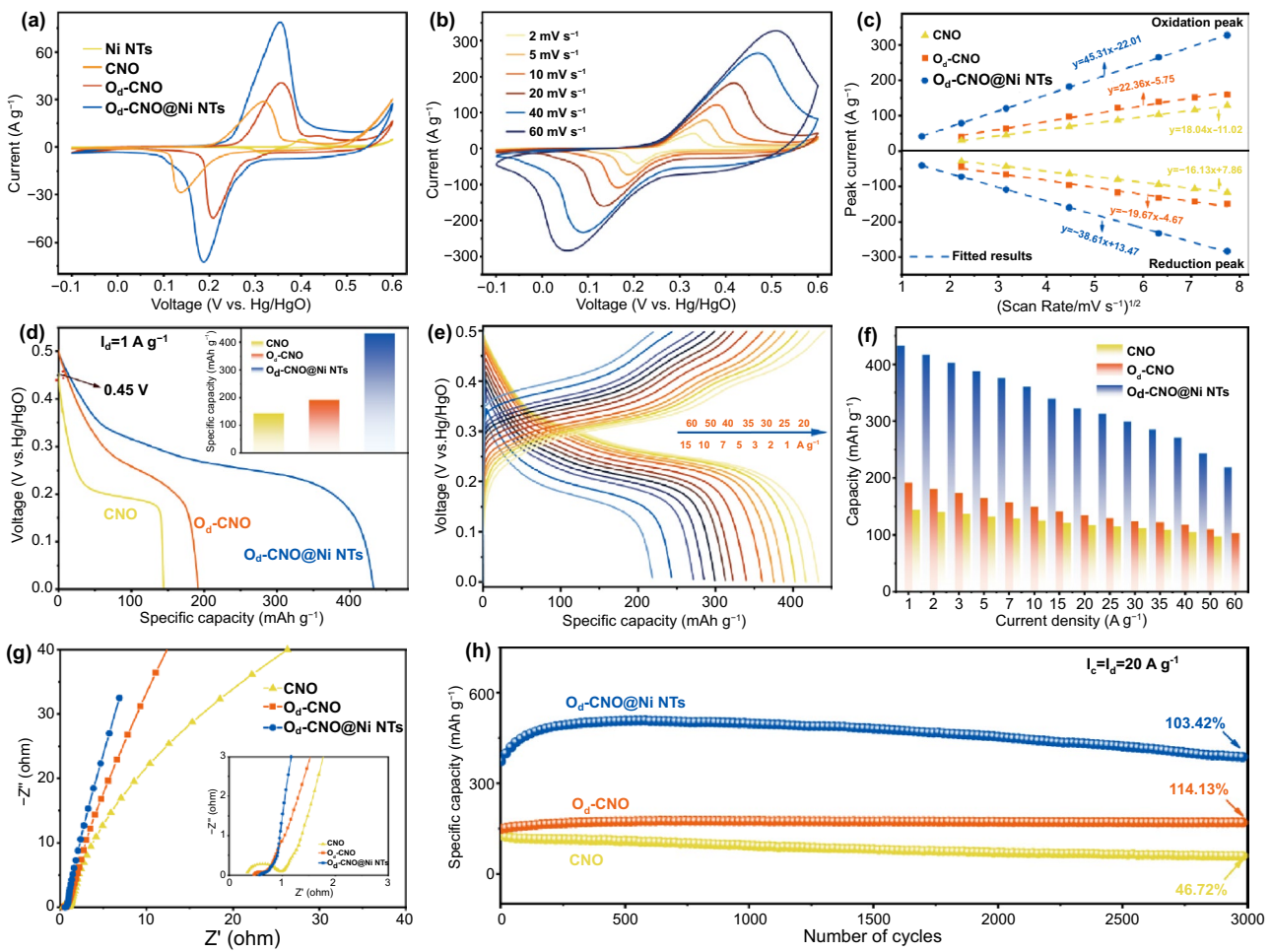


**Fig. 3** Electrochemical evaluation of the cathodes. **a** Comparison of CV. **b** CV of the  $O_d$ -CNO@Ni NTs at different scan rates. **c** Correlation between peak current and scan rate. **d** Discharge capacity of the  $O_d$ -CNO@Ni NTs,  $O_d$ -CNO and CNO at  $1 \text{ A g}^{-1}$ . **e** GCD of  $O_d$ -CNO@Ni NTs cathode. **f** Rate performance. **g** Nyquist plots. **h** Discharge capacity at  $20.0 \text{ A g}^{-1}$  for 3000 cycles

( $v^{1/2}$ ) is linear (Fig. 3c) [14]. Figure S10a–c shows the calculated contribution ratio of the three electrodes at various scan rates. For the  $O_d$ -CNO@Ni NTs electrode, 82% of the capacity is diffusive-controlled at  $5 \text{ mV s}^{-1}$  and gradually decreases to 51% at  $40 \text{ mV s}^{-1}$ , exhibiting the main diffusive-controlled behavior. For  $O_d$ -CNO electrode and CNO electrode, the capacitance contribution is more obvious. Therefore, the capacity decreases less as the current density increases, benefiting from the surface-control characteristics [33]. Electrochemical impedance spectroscopy (EIS) results also shed light on the enhanced electrochemical kinetics described above. Observed from the Nyquist plot (Fig. 3g), the corresponding equivalent circuit and its values are shown in Fig. S11 and Table S3. In the high-frequency region, a smaller semicircle (inset in Fig. 3g) is shown for  $O_d$ -CNO

and  $O_d$ -CNO@Ni NTs electrodes, and their charge transfer resistance  $R_{ct}$  ( $0.40 \text{ } \Omega$  of  $O_d$ -CNO,  $0.35 \text{ } \Omega$  of  $O_d$ -CNO@Ni NTs) is almost half of the CNO electrode ( $0.72 \text{ } \Omega$  of CNO). Furthermore, the slope of  $O_d$ -CNO and the  $O_d$ -CNO@Ni NTs is higher in the low frequency region, attributing to oxygen defects introduced in CNO to promote rapid charge transfer, improving the electrode conductivity during charging and discharging. Therefore, the  $O_d$ -CNO@Ni NTs electrode has an overwhelming advantage in terms of electrochemical performance.

Figure 3d shows the comparison of discharge behavior of CNO,  $O_d$ -CNO, and  $O_d$ -CNO@Ni NTs (at  $1 \text{ A g}^{-1}$ ). Compared with the CNO (0.45 V),  $O_d$ -CNO and  $O_d$ -CNO@Ni NTs electrodes (0.5 V) have a larger potential voltage

window (Fig. S12a–d). The  $O_d$ -CNO@Ni NTs electrode has a more ideal discharge potential platform. The specific capacity of  $O_d$ -CNO@Ni NTs electrodes is as high as  $432.7 \text{ mAh g}^{-1}$  (at  $1 \text{ A g}^{-1}$ ), significantly larger than that of  $O_d$ -CNO electrodes ( $191.8 \text{ mAh g}^{-1}$ ) and CNO electrodes ( $144.0 \text{ mAh g}^{-1}$ ). The GCD curves also indicate excellent charge storage capacity (Fig. 3e). The specific capacity reached 432.7, 416.4, 402.6, 387.7, 375.2, 360, 339.2, 322.3, 312.5, 299.2, 284.9, 271.1, 243, and  $218.3 \text{ mAh g}^{-1}$  at 1, 2, 3, 5, 7, 10, 15, 20, 25, 30, 35, 40, 50 and  $60 \text{ A g}^{-1}$ . The capacity of  $O_d$ -CNO@Ni NTs electrode still retains  $218.3 \text{ mAh g}^{-1}$  at  $60 \text{ A g}^{-1}$ , demonstrating an impressive rate performance. Comparing  $O_d$ -CNO and CNO electrodes (Figs. 3f and S13a–b), the capacity of  $O_d$ -CNO@Ni NTs electrodes is more than twice that of them, which once again proves the significant effect of hollow Ni NTs on increasing the specific capacity. Furthermore, to solve the main bottlenecks hindering the practical application of alkaline ZBBs, the cycle stability of the CNO,  $O_d$ -CNO, and  $O_d$ -CNO@Ni NTs electrode was evaluated (Fig. 3h). The  $O_d$ -CNO and  $O_d$ -CNO@Ni NTs electrodes showed impressive cycle capacity and structural stability after 3000 cycles (the capacity retention of the  $O_d$ -CNO and  $O_d$ -CNO@Ni NTs electrode were 114.1% and 103.4%, respectively), whereas the capacity retention of CNO electrodes is only 46.7% after 3000 cycles. This serious capacity degradation is related to the deactivation and self-dissolution of the electrode material itself. Importantly, the inductively coupled plasma optical emission spectrometry (ICP-OES) analysis of the Co concentration in electrolyte shows that the most Co ions were dissolved in CNO after 2000 cycles (Fig. S14). Figure S15 shows the SEM of  $O_d$ -CNO@Ni NTs,  $O_d$ -CNO and CNO electrodes at 100, 500, and 2000 cycles, respectively. After the long-cycle of different cycles, the morphology of CNO has obvious changes of dissolution, which eventually leads to the collapse of the structure and sharp attenuation of the capacity (Figs. S15c and S16a–b). However, the morphology of the  $O_d$ -CNO@Ni NTs and  $O_d$ -CNO electrode has no obvious change; thus, the structure is stable. It can still be observed that the clear and orderly hollow tubular structure and ultra-thin nanosheets are coated on the Ni NTs. This once again confirms that oxygen defects can significantly enhance the stability of the material, and abundant nickel nanotubes increase the capacity.

DFT calculation is used to study the impact of oxygen defects on the structure and electronic property. Based on the optimized  $O_d$ -CNO model, the adsorption behavior of  $\text{OH}^-$  was investigated, and the effects of electrochemical performances caused by defects were discussed (Fig. 4a). Two different  $\text{OH}^-$  adsorption sites on the defective surface were considered as shown in Fig. 4b. Apparently, compared with the pristine CNO as shown in Fig. 4c, the introduction of oxygen defects (point defect type/main lattice oxygen defect) can enhance the adsorption of  $\text{OH}^-$  with the decreased binding energies from  $-0.29$  to  $-3.18$  or  $-1.01 \text{ eV}$ , respectively, contributing to higher capacity and cycling stability of the electrode material. This is consistent with the above experimental analysis on the electrochemical performance. Meanwhile, from Bader analysis (Fig. 4b) [50], we found that the existence of oxygen defects could increase the charge transfer between electrode and  $\text{OH}^-$  from 0.57 to 0.64 or 0.61  $e^-$ , respectively, accounting for the improved adsorption of  $\text{OH}^-$  by oxygen defects.

To further discuss the charge storage mechanism, the total density of states (TDOS) of CNO bulk (Fig. S17), the TDOS of the pristine and  $O_d$ -CNO surface (Fig. 4d), and the partial density of states (PDOS) of the Ni-3d orbits (Fig. 4e) are calculated. From the TDOS of CNO bulk, CNO material has a metallic property, benefit for the charge transport during the electrode reactions. As the surface is the main place for redox reactions, the electronic properties of  $O_d$ -CNO surface are discussed. It can be seen that the empty band above the Fermi energy level is mainly contributed by Ni-3d orbits. After the generation of oxygen defects, the Fermi energy level shifts to a higher energy level, resulting in more empty states near the Fermi energy level. Therefore, these empty states could store more charges, leading to a higher capacity. The intermediate adsorption behavior of  $\text{OH}^-$  on the surface of the active material is very important for the reversible capacity of the electrode material [51]. With the combination of more available unoccupied states and the strong  $\text{OH}^-$  adsorption capacity, the Faraday reversible redox reaction will be promoted, thereby improving the charge storage capacity [52]. The theoretical calculation agrees with our experimental results, indicating that oxygen defects can effectively modify the surface electronic structure and improve the binding energy, rendering faster kinetics and better electrochemical performance.



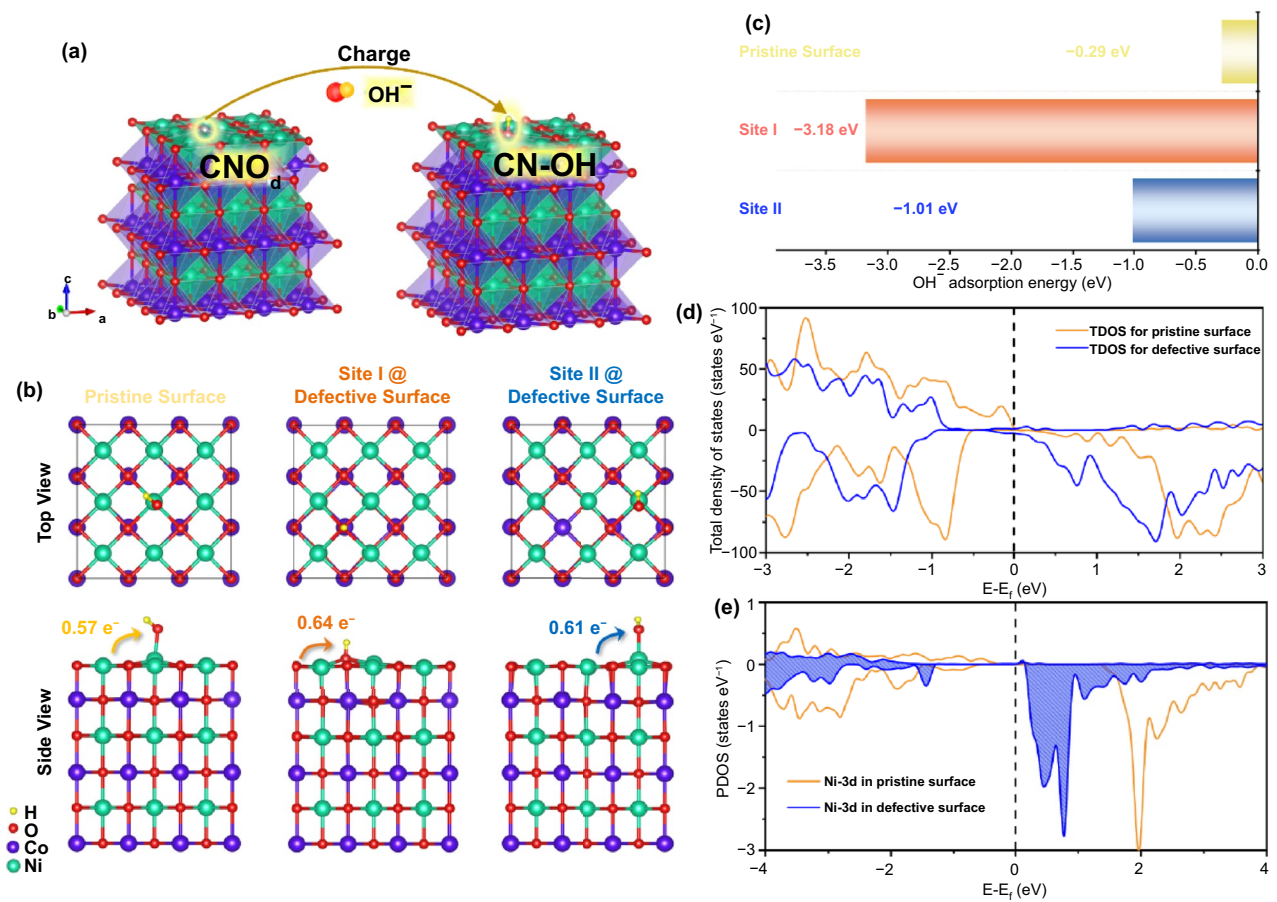


**Fig. 4** **a** Modulation mechanism model of oxygen defects on OH<sup>-</sup> adsorption. **b** Surface charge transfer and OH<sup>-</sup> adsorption energy analysis. **c** Adsorption energy of OH<sup>-</sup> on CNO and O<sub>d</sub>-CNO. **d** TDOS for CNO and O<sub>d</sub>-CNO. **e** PDOS for CNO and O<sub>d</sub>-CNO

### 3.3 Evaluation of the O<sub>d</sub>-CNO@Ni NTs//Zn Aqueous Battery

We use the O<sub>d</sub>-CNO@Ni NTs and zinc foil as cathode and counter electrode, the actual performance of the battery was evaluated in 4 M KOH + 2 M KF + 1 M K<sub>2</sub>CO<sub>3</sub> + Sat. ZnO

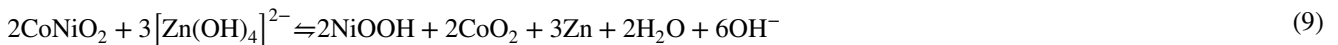
Cathode:



Anode:



Overall:



electrolyte. To explore the energy storage mechanism of O<sub>d</sub>-CNO@Ni NTs//Zn battery, we conducted a series of ex situ tests, such as ex situ SEM (Fig. S18), ex situ XRD (Fig. S19), ex situ XPS (Fig. S20), and ex situ TEM (Fig. S21). The mechanism of the battery can be understood as following equation [19, 22–25]:

Figure 5a illustrates the CV of 1–30 mV s<sup>-1</sup> (1.2–2 V) for O<sub>d</sub>-CNO@Ni NTs//Zn aqueous battery. At 1 mV s<sup>-1</sup>, the O<sub>d</sub>-CNO@Ni NTs//Zn battery exhibits good symmetrical redox peaks (1.81/1.64 V). Even at 30 mV s<sup>-1</sup>, it still remains symmetric (1.96/1.52 V), which means that the battery has excellent reversibility. Meanwhile, the form of the CV curve remained almost does not change at different scanning rates

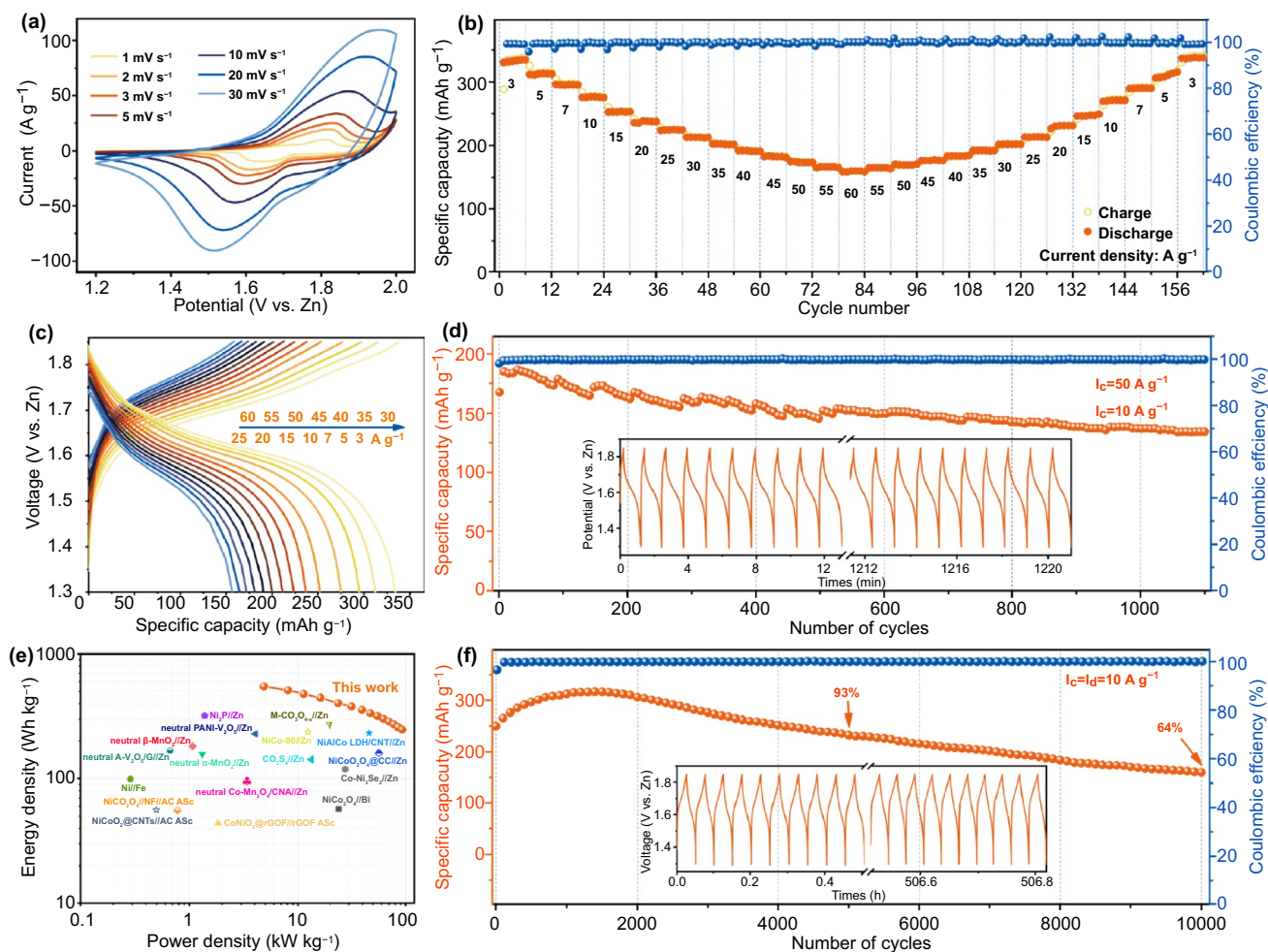


**Fig. 5** Electrochemical performance of the battery. **a** CV profiles. **b** Rate performance and coulombic efficiency. **c** GCD curves. **d** Cyclic performance and coulomb efficiency at fast charge and slow discharge. The illustration displays the time–voltage curves at the first and last 10 cycles. **e** Ragone plot comparing the performance values of the  $O_4$ -CNO@Ni NTs//Zn battery with those of other ZBBs. **f** Cycling performance of the Ni//Zn battery. The illustration displays the time–voltage curves at the first and last 10 cycles

(1–30  $mV s^{-1}$ ), proving the battery has excellent stability. Figure 5b shows the battery's rate capability and coulomb efficiency. The extremely high coulombic efficiency indicates that the battery is ability of rapid charge transfer and ion diffusion. Importantly, the  $O_4$ -CNO@Ni NTs//Zn battery exhibits high capacity of 334.9, 313.4, 296.3, 277.0, 253.3, 238.3, 225.0, 212.5, 202.2, 192.2, 183.8, 175.0, 166.5, and 160.0  $mAh g^{-1}$  when at 3, 5, 7, 10, 15, 20, 25, 30, 35, 40, 45, 50, 55, and 60  $A g^{-1}$ , respectively. The average discharge capacity can be restored when switching to 3  $A g^{-1}$  after 156 cycles, which indicates that  $O_4$ -CNO@Ni NTs//Zn battery has an extraordinary rate and reversible stability. Figure 5c shows the GCD curve of the  $O_4$ -CNO@Ni NTs//Zn battery

at different current density, showing a flat output voltage (1.62 V). The  $O_4$ -CNO@Ni NTs//Zn aqueous battery can be effectively charged/discharged in about 9.5 s at an extremely high current density (Fig. S22). It still maintains a high capacity of 158.3  $mAh g^{-1}$  (at 60  $A g^{-1}$ ), implying its ultra-fast properties, providing the possibility of achieving fast charging. Further, Fig. 5d is a graph of the cycle performance of the  $O_4$ -CNO@Ni NTs//Zn battery under fast charge (50  $A g^{-1}$ ) and slow discharge (10  $A g^{-1}$ ) conditions. After 1100 cycles (approximately 20.3 h), the capacity retention still exceeded 80%. Comparing the GCD curve before and after the cycle (inset in Fig. 5d), there is no obvious change before and after the cycle, indicating the excellent

stability of  $O_d$ -CNO@Ni NTs//Zn battery under fast charge and slow discharge. It again demonstrates that hollow nickel nanotubes and abundant oxygen defects enhance the stability of the material during rapid charging and slow discharge repeatedly. Such excellent performance is almost unreported in current ZBBs.

An ultra-long cycle is realized in the  $O_d$ -CNO@Ni NTs//Zn battery (Fig. 5f). After multiple electrochemical activations, the coulombic efficiency remains nearly 100%. Moreover, as calculated, after 5000 cycles, the  $O_d$ -CNO@Ni NTs//Zn battery at  $10 \text{ A g}^{-1}$  with a capacity of  $232.7 \text{ mAh g}^{-1}$ , which is 93% of the initial average capacity. After 10,000 cycles (approximately 22 days), the cycle stability reached 64%. Furthermore, the Ragone plot compares  $O_d$ -CNO@Ni NTs//Zn battery with the most

advanced aqueous electrochemical system. Encouragingly, in Fig. 5e, our work proposes a maximum energy density is  $547.5 \text{ Wh kg}^{-1}$  (based on the mass of the  $O_d$ -CNO@Ni NTs cathode), and a maximum power density is  $92.9 \text{ kW kg}^{-1}$ . This performance is better than almost all reported aqueous ZBBs, including, alkaline Ni–Zn [53], Co–Zn [19], Ni–Bi [54], Ni–Fe batteries [55], neutral Zn–Mn [56], Zn–V batteries [57]. Besides, we noticed that supercapacitors also use nickel and cobalt bases as cathodes. In contrast, the energy density of supercapacitors is very low [58].

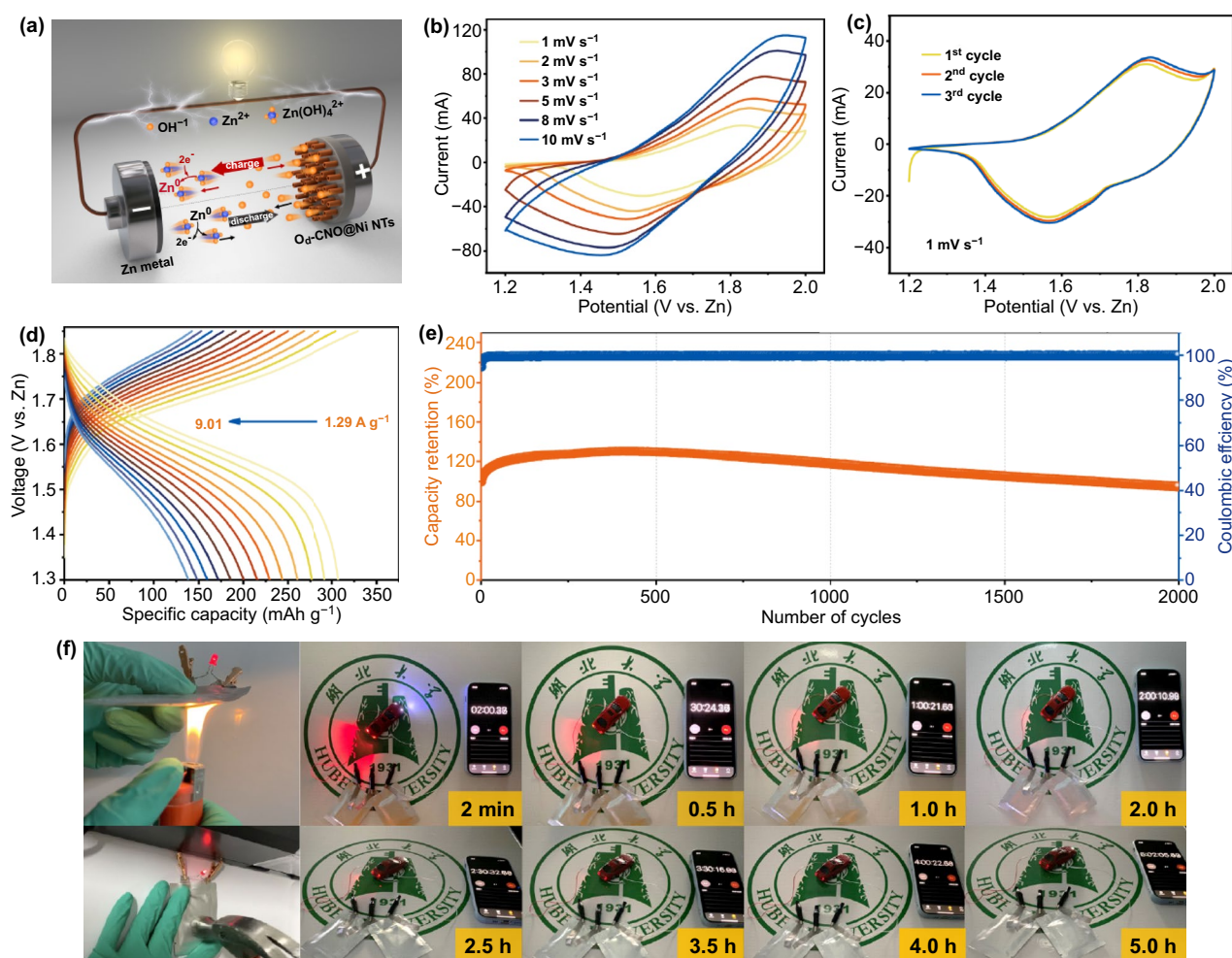


**Fig. 6** **a** Schematic illustration of the  $O_d$ -CNO@Ni NTs//Zn battery. The  $O_d$ -CNO@Ni NTs//Zn soft-pack battery **b** CV profiles. **c** CV curves for the first three cycles at  $1 \text{ mV s}^{-1}$ . **d** GCD profiles. **e** Cycle stability at  $5 \text{ A g}^{-1}$ . **f** Photograph of safety tests and powering a 3 V model car

### 3.4 Evaluation of the O<sub>d</sub>-CNO@Ni NTs//Zn Soft-Pack Battery

Finally, in order to verify the possibility of application in real life, a soft-pack O<sub>d</sub>-CNO@Ni NTs//Zn battery was prepared. The configuration illustration of soft-pack battery is shown in Fig. 6a. As shown in the CV curves in Fig. 6b, c and S23, the redox peak represents the electrochemical process. The soft-pack battery is also capable of achieving high rate performance and long cycle life. At the current density of 1.29, 1.93, 2.58, 3.22, 3.86, 4.51, 5.15, 5.79, 6.44, 7.08, 7.73, 8.37, and 9.01 A g<sup>-1</sup>, the high capacity of 307.22, 291.84, 276.25, 260.19, 243.56, 229.07, 216.02, 199.89, 185.44, 171.72, 159.44, 148.08, and 138.19 mAh g<sup>-1</sup>, respectively (Fig. 6d). The capacity retention is still above 90% after 2000 cycles at 5 A g<sup>-1</sup> (Fig. 6e). As a result, 3 V car lights are selected as the load for the two series soft-pack batteries. The car lights are very bright and can be kept on for more than 5 h (Fig. 6f). More importantly, comparing the CV before and after exposure to fire and hammer (Fig. S24a–b), the soft-pack battery can work continuously and stably under fire and hammer test (Fig. 6f, Videos S1 and S2). No danger of fire and blast, showing excellent reliability and security.

## 4 Conclusion

In summary, this work developed a three-dimensional hierarchical structure with ordered vertical nanotubes arrays and defective nanosheets, which greatly enhanced the electrochemical performance. Specifically, the existence of Ni NTs can increase ion diffusion channels and shorten ion migration distance, thereby having high conductivity and abundant active sites. More importantly, oxygen defects effectively improve the electrochemical kinetics of the cathode, make the electrode maintain good reversibility for a long time, and improve the surface electronic state structure of O<sub>d</sub>-CNO @ Ni NTs, thus exhibiting strong OH<sup>-</sup> adsorption capacity. As a result, the O<sub>d</sub>-CNO@Ni NTs cathode shows improved specific capacity (432.7 mAh g<sup>-1</sup>) and extraordinary rate performance (218.3 mAh g<sup>-1</sup> at 60 A g<sup>-1</sup>). The capacity of the prepared O<sub>d</sub>-CNO@Ni NTs//Zn rechargeable battery is 334.9 mAh g<sup>-1</sup>, and the cycling stability is 93%. At the

same time, it still has a capacity retention of 80% under the condition of fast charge (50 A g<sup>-1</sup>) and slow discharge (10 A g<sup>-1</sup>) after 1100 cycles. Our battery can also work at high temperature and high pressure, which will bring immediate benefits to the development for next-generation high-safety commercial batteries.

**Acknowledgements** This work was supported by the National Natural Science Foundation of China (No. 52002122), the Science and Technology Department of Hubei Province (No. 2019AAA038), the Project funded by China Postdoctoral Science Foundation (No. 2021M690947) and the Wuhan Yellow Crane Talent Program (No. 2017-02).

**Open Access** This article is licensed under a Creative Commons Attribution 4.0 International License, which permits use, sharing, adaptation, distribution and reproduction in any medium or format, as long as you give appropriate credit to the original author(s) and the source, provide a link to the Creative Commons licence, and indicate if changes were made. The images or other third party material in this article are included in the article's Creative Commons licence, unless indicated otherwise in a credit line to the material. If material is not included in the article's Creative Commons licence and your intended use is not permitted by statutory regulation or exceeds the permitted use, you will need to obtain permission directly from the copyright holder. To view a copy of this licence, visit <http://creativecommons.org/licenses/by/4.0/>.

**Supplementary Information** The online version contains supplementary material available at <https://doi.org/10.1007/s40820-021-00699-z>.

## References

1. B. Dunn, H. Kamath, J.M. Tarascon, Electrical energy storage for the grid: a battery of choices. *Science* **334**, 928–935 (2011). <https://doi.org/10.1126/science.1212741>
2. Z.P. Cano, D. Banham, S. Ye, A. Hintennach, J. Lu et al., Batteries and fuel cells for emerging electric vehicle markets. *Nat. Energy* **3**, 279–289 (2018). <https://doi.org/10.1038/s41560-018-0108-1>
3. L. Shan, S. Liang, B. Tang, J. Zhou, Development and challenges of aqueous rechargeable zinc batteries. *Sci. Bull.* **65**, 3562–3584 (2020). <https://doi.org/10.1360/TB-2020-0352>
4. D. Chao, W. Zhou, F. Xie, C. Ye, H. Li et al., Roadmap for advanced aqueous batteries: from design of materials to applications. *Adv. Sci.* **6**, eaba4098 (2020). <https://doi.org/10.1126/sciadv.aba4098>
5. H. Li, D. Chao, B. Chen, X. Chen, C. Chuah et al., Revealing principles for design of lean-electrolyte lithium metal anode via in situ spectroscopy. *J. Am. Chem. Soc.* **142**, 2012–2022 (2020). <https://doi.org/10.1021/jacs.9b11774>
6. C. Ye, Y. Jiao, D. Chao, T. Ling, J. Shan et al., Electron-state confinement of polysulfides for highly stable sodium-sulfur

- batteries. *Adv. Mater.* **32**, 1907557–1907564 (2020). <https://doi.org/10.1002/adma.201907557>
7. J. Huang, J. Zhou, S. Liang, Guest pre-intercalation strategy to boost the electrochemical performance of aqueous zinc-ion battery cathodes. *Acta Phys. Chim. Sin.* **37**, 2005020 (2021). <https://doi.org/10.3866/PKU.WHXB202005020>
  8. J. Gao, X. Xie, S. Liang, B. Lu, J. Zhou, Inorganic colloidal electrolyte for highly robust zinc-ion batteries. *Nano-Micro Lett.* **13**, 1 (2021). <https://doi.org/10.1007/s40820-020-00525-y>
  9. G.G. Yadav, J.W. Gallaway, D.E. Turney, M. Nyce, J. Huang et al., Regenerable Cu-intercalated MnO<sub>2</sub> layered cathode for highly cyclable energy dense batteries. *Nat. Commun.* **8**, 14424 (2017). <https://doi.org/10.1038/ncomms14424>
  10. C. Li, Q. Zhang, J. Sun, T. Li, S. Eagan et al., High-performance quasi-solid-state flexible aqueous rechargeable Ag–Zn battery based on metal–organic framework-derived Ag nanowires. *ACS Energy Lett.* **3**, 2761–2768 (2018). <https://doi.org/10.1021/acseenergylett.8b01675>
  11. Y. Jian, D. Wang, M. Huang, H.-L. Jia, J. Sun et al., Facile synthesis of Ni(OH)<sub>2</sub>/carbon nanofiber composites for improving nzn battery cycling life. *ACS Sustain. Chem. Eng.* **5**, 6827–6834 (2017). <https://doi.org/10.1021/acssuschemeng.7b01048>
  12. C. Xu, J. Liao, C. Yang, R. Wang, D. Wu et al., An ultrafast, high capacity and superior longevity Ni/Zn battery constructed on nickel nanowire array film. *Nano Energy* **30**, 900–908 (2016). <https://doi.org/10.1016/j.nanoen.2016.07.035>
  13. X. Wang, M. Li, Y. Wang, B. Chen, Y. Zhu et al., A Zn–NiO rechargeable battery with long lifespan and high energy density. *J. Mater. Chem. A* **3**, 8280–8283 (2015). <https://doi.org/10.1039/C5TA01947H>
  14. W. Zhou, J. He, D. Zhu, J. Li, Y. Chen, Hierarchical NiSe<sub>2</sub> nanosheet arrays as a robust cathode toward superdurable and ultrafast Ni–Zn aqueous batteries. *ACS Appl. Mater. Interfaces* **12**, 34931–34940 (2020). <https://doi.org/10.1021/acami.0c08205>
  15. P. Hu, T. Wang, J. Zhao, C. Zhang, J. Ma et al., Ultrafast alkaline Ni/Zn battery based on Ni-foam-supported Ni<sub>3</sub>S<sub>2</sub> nanosheets. *ACS Appl. Mater. Interfaces* **7**, 26396–26399 (2015). <https://doi.org/10.1021/acami.5b09728>
  16. L. Zhou, X. Zhang, D. Zheng, W. Xu, J. Liu et al., Ni<sub>3</sub>S<sub>2</sub>@PANI core–shell nanosheets as a durable and high-energy binder-free cathode for aqueous rechargeable nickel–zinc batteries. *J. Mater. Chem. A* **7**, 10629–10635 (2019). <https://doi.org/10.1039/C9TA00681H>
  17. Z. Lu, X. Wu, X. Lei, Y. Li, X. Sun, Hierarchical nanoarray materials for advanced nickel–zinc batteries. *Inorg. Chem. Front.* **2**, 184–187 (2015). <https://doi.org/10.1039/C4QI00143E>
  18. X. Wang, F. Wang, L. Wang, M. Li, Y. Wang et al., An aqueous rechargeable Zn//Co<sub>3</sub>O<sub>4</sub> battery with high energy density and good cycling behavior. *Adv. Mater.* **28**, 4904–4911 (2016). <https://doi.org/10.1002/adma.201505370>
  19. C. Teng, F. Yang, M. Sun, K. Yin, Q. Huang et al., Structural and defect engineering of cobaltic oxide nanoarchitectures as an ultrahigh energy density and super durable cathode for Zn-based batteries. *Chem. Sci.* **10**, 7600–7609 (2019). <https://doi.org/10.1039/C9SC01902B>
  20. S. Zhang, B. Yin, Y. Luo, L. Shen, B. Tang et al., Fabrication and theoretical investigation of cobaltic sulfide nanosheets for flexible aqueous Zn/Co batteries. *Nano Energy* **68**, 104314 (2019). <https://doi.org/10.1016/j.nanoen.2019.104314>
  21. H. Chen, Z. Shen, Z. Pan, Z. Kou, X. Liu et al., Hierarchical micro-nano sheet arrays of nickel-cobalt double hydroxides for high-rate Ni–Zn batteries. *Adv. Sci.* **6**, 1802002 (2019). <https://doi.org/10.1002/advsc.201802002>
  22. W. He, S. Wang, Y. Shao, Z. Kong, H. Tu et al., Water invoking interface corrosion: an energy density booster for Ni//Zn battery. *Adv. Energy Mater.* **11**, 2003268 (2021). <https://doi.org/10.1002/aenm.202003268>
  23. Y. Zeng, Z. Lai, Y. Han, H. Zhang, S. Xie et al., Oxygen-vacancy and surface modulation of ultrathin nickel cobaltite nanosheets as a high-energy cathode for advanced Zn-ion batteries. *Adv. Mater.* **30**, 1802396 (2018). <https://doi.org/10.1002/adma.201802396>
  24. W. Shang, W. Yu, P. Tan, B. Chen, H. Xu et al., A high-performance Zn battery based on self-assembled nanostructured NiCo<sub>2</sub>O<sub>4</sub> electrode. *J. Power Sources* **421**, 6–13 (2019). <https://doi.org/10.1016/j.jpowsour.2019.02.097>
  25. H. Zhang, X. Zhang, H. Li, Y. Zhang, Y. Zeng et al., Flexible rechargeable Ni//Zn battery based on self-supported NiCo<sub>2</sub>O<sub>4</sub> nanosheets with high power density and good cycling stability. *Green Energy Environ.* **3**, 56–62 (2018). <https://doi.org/10.1016/j.gee.2017.09.003>
  26. J.F. Parker, C.N. Chervin, I.R. Pala, M. Machler, M.F. Burz et al., Rechargeable nickel–3D zinc batteries: an energy-dense, safer alternative to lithium-ion. *Science* **356**, 415–418 (2017). <https://doi.org/10.1126/science.aak9991>
  27. H. Li, L. Ma, C. Han, Z. Wang, Z. Liu et al., Advanced rechargeable zinc-based batteries: recent progress and future perspectives. *Nano Energy* **62**, 550–587 (2019). <https://doi.org/10.1016/j.nanoen.2019.05.059>
  28. M. Huang, M. Li, C. Niu, Q. Li, L. Mai, Recent advances in rational electrode designs for high-performance alkaline rechargeable batteries. *Adv. Funct. Mater.* **29**, 1807847 (2019). <https://doi.org/10.1002/adfm.201807847>
  29. Q.N. Zhu, Z.Y. Wang, J.W. Wang, X.Y. Liu, D. Yang et al., Challenges and strategies for ultrafast aqueous zinc-ion batteries. *Rare Met.* **40**, 309–328 (2020). <https://doi.org/10.1007/s12598-020-01588-x>
  30. W. Zhou, D. Zhu, J. He, J. Li, H. Chen et al., A scalable top-down strategy toward practical metrics of Ni–Zn aqueous batteries with total energy densities of 165 wh kg<sup>-1</sup> and 506 wh L<sup>-1</sup>. *Energy Environ. Sci.* **13**, 4157–4167 (2020). <https://doi.org/10.1039/D0EE01221A>
  31. J. Ji, H. Wan, B. Zhang, C. Wang, Y. Gan et al., Co<sup>2+</sup>/<sup>3+</sup>/<sup>4+</sup>-regulated electron state of Mn–O for superb aqueous zinc-manganese oxide batteries. *Adv. Energy Mater.* **11**, 2003203 (2020). <https://doi.org/10.1002/aenm.202003203>
  32. Y. Zhang, L. Tao, C. Xie, D. Wang, Y. Zou et al., Defect engineering on electrode materials for rechargeable



- batteries. *Adv. Mater.* **32**, 1905923 (2020). <https://doi.org/10.1002/adma.201905923>
33. W. Liu, Y. Chen, Y. Wang, Q. Zhao, L. Chen et al., Influence of anion substitution on 3D-architected Ni-Co-A (A = H, O, P) as efficient cathode materials towards rechargeable Zn-based battery. *Energy Storage Mater.* **37**, 336–344 (2021). <https://doi.org/10.1016/j.ensm.2021.02.026>
34. G. Kresse, J. Hafner, Ab initio molecular-dynamics simulation of the liquid–metal–amorphous–semiconductor transition in germanium. *Phys. Rev. B* **49**, 14251–14269 (1994). <https://doi.org/10.1103/PhysRevB.49.14251>
35. P. Hohenberg, W. Kohn, Inhomogeneous electron gas. *Phys. Rev.* **136**, B864–B871 (1964). <https://doi.org/10.1103/PhysRev.136.B864>
36. W. Kohn, L.J. Sham, Self-consistent equations including exchange and correlation effects. *Phys. Rev.* **140**, A1133–A1138 (1965). <https://doi.org/10.1103/PhysRev.140.A1133>
37. J.P. Perdew, K. Burke, M. Ernzerhof, Generalized gradient approximation made simple. *Phys. Rev. Lett.* **77**, 3865–3868 (1998). <https://doi.org/10.1103/PhysRevLett.77.3865>
38. A.I. Liechtenstein, V.V. Anisimov, J. Zaanen, Density-functional theory and strong interactions: orbital ordering in mott-hubbard insulators. *Phys. Rev. B* **52**, R5467–R5470 (1995). <https://doi.org/10.1103/PhysRevB.52.R5467>
39. S.L. Dudarev, A.I. Liechtenstein, M.R. Castell, G. Briggs, A.P. Sutton, Surface states on NiO(100) and the origin of the contrast reversal in atomically resolved scanning tunneling microscope images. *Phys. Rev. B* **56**, 4900 (1997). <https://doi.org/10.1103/PhysRevB.56.4900>
40. A. Jain, G. Hautier, C.J. Moore, S. Ping Ong, C.C. Fischer et al., A high-throughput infrastructure for density functional theory calculations. *Comput. Mater. Sci.* **50**, 2295–2310 (2011). <https://doi.org/10.1016/j.commatsci.2011.02.023>
41. S. Grimme, J. Antony, S. Ehrlich, H. Krieg, A consistent and accurate ab initio parametrization of density functional dispersion correction (DFT-D) for the 94 elements H–Pu. *J. Chem. Phys.* **132**, 154104 (2010). <https://doi.org/10.1063/1.3382344>
42. H.J. Monkhorst, J.D. Pack, Special points for brillouin-zone integrations. *Phys. Rev. B* **13**, 5188–5192 (1976). <https://doi.org/10.1103/PhysRevB.13.5188>
43. K. Momma, F. Izumi, Vesta: a three-dimensional visualization system for electronic and structural analysis. *J. Appl. Crystallogr.* **41**, 653–658 (2008). <https://doi.org/10.1107/S0021889808012016>
44. S.H. Kim, J.M. Kim, D.B. Ahn, S.Y. Lee, Cellulose nanofiber/carbon nanotube-based bicontinuous ion/electron conduction networks for high-performance aqueous Zn-ion batteries. *Small* **16**, 2002837 (2020). <https://doi.org/10.1002/sml.202002837>
45. C. Hu, L. Miao, Q. Yang, X. Yu, L. Song et al., Self-assembly of CNTs on Ni foam for enhanced performance of NiCoO<sub>2</sub>@CNT@NF supercapacitor electrode. *Chem. Eng. J.* **410**, 128317 (2020). <https://doi.org/10.1016/j.cej.2020.128317>
46. L. Kang, M. Zhang, J. Zhang, S. Liu, N. Zhang et al., Dual-defect surface engineering of bimetallic sulfide nanotubes towards flexible asymmetric solid-state supercapacitors. *J. Mater. Chem. A* **8**, 24053–24064 (2020). <https://doi.org/10.1039/D0TA08979F>
47. C. Wang, Z. Song, H. Wan, X. Chen, Q. Tan et al., Ni–Co selenide nanowires supported on conductive wearable textile as cathode for flexible battery-supercapacitor hybrid devices. *Chem. Eng. J.* **400**, 125955 (2020). <https://doi.org/10.1016/j.cej.2020.125955>
48. X. Zhang, F. Yang, H. Chen, K. Wang, J. Chen et al., In situ growth of 2D ultrathin NiCo<sub>2</sub>O<sub>4</sub> nanosheet arrays on Ni foam for high performance and flexible solid-state supercapacitors. *Small* **16**, 2004188 (2020). <https://doi.org/10.1002/sml.202004188>
49. Q. Tan, X. Li, B. Zhang, X. Chen, Y. Tian et al., Valence engineering via in situ carbon reduction on octahedron sites Mn<sub>3</sub>O<sub>4</sub> for ultra-long cycle life aqueous Zn-ion battery. *Adv. Energy Mater.* **10**, 2001050 (2020). <https://doi.org/10.1002/aenm.202001050>
50. R.F.W. Bader, *Atoms in Molecules: A Quantum Theory* (Oxford University Press, Oxford, 1990)
51. X. Zhao, H. Wan, P. Liang, N. Wang, C. Wang et al., Favorable anion adsorption/desorption of high rate NiSe<sub>2</sub> nanosheets/hollow mesoporous carbon for battery-supercapacitor hybrid devices. *Nano Res.* **66**, 1–10 (2020). <https://doi.org/10.1007/s12274-020-3257-z>
52. Y. Gan, C. Wang, X. Chen, P. Liang, H. Wang, High conductivity Ni<sub>12</sub>P<sub>5</sub> nanowires as high-rate electrode material for battery-supercapacitor hybrid devices. *Chem. Eng. J.* **392**, 123661 (2019). <https://doi.org/10.1016/j.cej.2019.123661>
53. M. Gong, Y. Li, H. Zhang, B. Zhang, W. Zhou et al., Ultrafast high-capacity NiZn battery with NiAlCo-layered double hydroxide. *Energy Environ. Sci.* **7**, 2025–2032 (2014). <https://doi.org/10.1039/C4EE00317A>
54. Y. Zeng, Z. Lin, Y. Meng, Y. Wang, M. Yu et al., Flexible ultrafast aqueous rechargeable Ni//Bi battery based on highly durable single-crystalline bismuth nanostructured anode. *Adv. Mater.* **28**, 9188–9195 (2016). <https://doi.org/10.1002/adma.201603304>
55. J. Liu, M. Chen, L. Zhang, J. Jiang, J. Yan et al., A flexible alkaline rechargeable Ni/Fe battery based on graphene foam/carbon nanotubes hybrid film. *Nano Lett.* **14**, 7180–7187 (2014). <https://doi.org/10.1021/nl503852m>
56. H. Pan, Y. Shao, P. Yan, Y. Cheng, K.S. Han et al., Reversible aqueous zinc/manganese oxide energy storage from conversion reactions. *Nat. Energy* **1**, 1–7 (2016). <https://doi.org/10.1038/nenergy.2016.39>
57. S. Liu, H. Zhu, B. Zhang, G. Li, H. Zhu et al., Tuning the kinetics of zinc-ion insertion/extraction in V<sub>2</sub>O<sub>5</sub> by in situ polyaniline intercalation enables improved aqueous zinc-ion storage performance. *Adv. Mater.* **32**, 2001113 (2020). <https://doi.org/10.1002/adma.202001113>
58. X. Jiang, Z. Li, G. Lu, N. Hu, G. Ji et al., Pores enriched CoNiO<sub>2</sub> nanosheets on graphene hollow fibers for high performance supercapacitor-battery hybrid energy storage. *Electrochim. Acta* **358**, 136857 (2020). <https://doi.org/10.1016/j.electacta.2020.136857>